Tailoring Electronic Transparency of Twin-Plane 1D Superlattices

Helio Tsuzuki, Daniel Ferreira Cesar, Mariama Rebello de Sousa Dias, Leonardo Kleber Castelano, Victor Lopez-Richard, José Pedro Rino, and Gilmar Eugenio Marques*

Departamento de Física, Universidade Federal de São Carlos, 13.565-905, São Carlos, São Paulo, Brazil

ABSTRACT The structural properties of twin-plane superlattices in InP nanowires are systematically analyzed. First, we employ molecular dynamics simulations to determine the strain fields in nanowires grown in the [111] direction. These fields are produced by the formation of twin-planes and by surface effects. By using the stress tensor obtained from molecular dynamics simulations, we are able to describe changes on the electronic structure of these nanowires. On the basis of the resulting electronic structure, we confirm that a one-dimensional superlattice is indeed formed. Furthermore, we describe the transport properties of both electrons and holes in the twin-plane superlattices. In contrast to the predicted transparency of Γ-electrons in heterolayered III−V semiconductor superlattices, we verify that surface effects in 1D systems open up possibilities of electronic structure engineering and the modulation of their transport and optical responses.

KEYWORDS: nanowire · InP · twin plane · superlattice · transparency · transport

Exploring functional nanotechnology has become a central task in recent research endeavors given the advances attained in the synthesis of nanomaterials. In particular, nanowires (NWs) have attracted increasing interest due to their potential application as optically active devices[1] and as building blocks for nanocircuits.[2] The technological advantage of NWs is related to the ability of engineering and controlling their quantum properties which can be achieved, for instance, through the modification of the NW geometry and strain fields.[3,4] On the other hand, the plausibility of building inhomogeneous heterostructures of a single semiconductor material was long ago theoretically predicted, when stacking faults and the creation of layered systems of semiconductor segments between twin-planes were simulated.[5] There is however a major shortcoming in the effective use of twin-planes for quantum effects in zincblende heterostructures: the mere presence of a twin stacking fault would not practically affect the transmission of Γ-electrons and these interfaces would remain mostly transparent.[6,7] Just recently, the controlled synthesis of stacking fault heterostructures of III−V compound semiconductor NWs has been reported.[8,9] It was shown that by controlling either the growth temperature and diameter of InAs NWs[8] or the amount of impurity dopants in analogous InP systems,[9] a periodic twin-plane structure can be experimentally realized. Such a microscopic control of the crystalline structure during the NW synthesis would open up opportunities for a thorough modulation of their electronic structure, thus increasing the potential use of these NWs as quantum heterodevices.

In this work, we report a systematic study about the microscopic structure of NWs, the formation of their peculiar strain fields affected by the surface and by twin-plane interfaces, and how they influence the electronic structure and transport properties of Γ-electrons and holes. There is a vast literature about simulations of InP NWs. For instance, *ab initio* calculations were performed to study the stability of the NWs grown along the [111] direction as a function of the diameter,[10] the change on the total energy due to defects,[11] the influence of hydrogen and oxygen on the surface of InP NWs,[12] and the stability of InP NWs with zincblende and wurtzite structures.[13] Furthermore, Monte Carlo calculations were used by Sano *et al.*[14] to understand the formation of the twin-planes and the tight-binding model was applied by Persson and Xu[15] to study InP NWs with orientation [100]. More recently, the band structure of twin-plane NWs was theoretically obtained within the framework of density functional theory.[16,17] These calculations also show that there is indeed a possibility of band engineering on polytypic superlattices with alternate zincblende and wurtzite crystalline phases, with band-offsets up to 90 meV.

In our case, we study the properties of InP zincblende type NWs by employing molecular dynamics (MD) simulations combined with a multiband electronic structure calculation, and we analyze the electronic transport within the envelope function approximation. The advantage of using MD is

* Address correspondence to gemarques@df.ufscar.br.

Received for review March 4, 2011 and accepted June 11, 2011.

Published online June 12, 2011
10.1021/nn2008589

related to the capacity to simulate real size NWs and to extract mechanical properties, which are used as input data to the multiband calculation. Interestingly, the variation of the band structure in this work is only due to strain fields caused by the formation of the twin-planes and the peculiar surface, differently from the case where polytypic phases are present.[16,17] On the basis of the band structure results, we are able to calculate the transport properties of the twin-plane superlattice through the transfer matrix method.[18] Furthermore, we analyze the transport of both types of carriers: electrons and holes. This consideration is important because the transparency or opaqueness of a twin-plane superlattice is directly associated to the carrier character (controlled by the strain conditions), as demonstrated by our results.

RESULTS AND DISCUSSION

In this work, we simulate two InP NWs with different cross sections and with the same shape as reported in refs 8 and 9. From the computationally simulated atomic structure of these NWs, we are able to extract the values of the elastic properties (elastic constants at $T = 0$ K) and strain profiles (with and without external stress). Such results are used as input parameters for the electronic structure calculation and the subsequent simulation of the electronic transport within the conduction and valence bands. In the following subsections, we describe in detail how we use molecular dynamics to simulate InP NWs and how we extract the interface effects, which cannot be obtained through empirical methods (*e.g.*, tight-binding and $\mathbf{k}\cdot\mathbf{p}$). Also, we show how the strain fields are included in the $\mathbf{k}\cdot\mathbf{p}$ Hamiltonian along [111] direction. After that, we calculate the electronic structure of the twin-plane InP NWs, which is the basis to determine the transport properties. Along with the description of the methods employed in this work, we also present and discuss the results in the subsections.

Molecular Dynamics. Indium phosphide, as several other III−V semiconductors, crystallizes in a cubic zincblende structure, where each atom is tetrahedrally bonded to their nearest neighbor through different percentages of covalent and ionic bonds. To simulate a twin-plane nanowire, the atomic positions for a given number of atoms are generated considering the *x*, *y*, and *z* axis parallel to the crystallographic directions $[2\bar{1}\bar{1}]$, $[01\bar{1}]$, and [111], respectively. To make an atomistic simulation of the NWs, we assume an effective interatomic potential that considers two- and three-body interactions having the same functional form as proposed by Ebbsjo *et al.*[19] By using this interaction potential, Branicio *et al.*[20] were able to describe the thermodynamical properties, structural phase transformation induced by pressure, elastic constants, stacking faults, and surface energies for bulk InP. However, to reproduce the experimental elastic

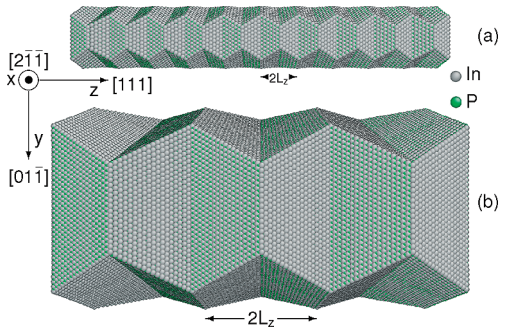

Figure 1. Molecular dynamics simulation of NWs after undergoing relaxation and thermalization processes. The results for the NW1 (NW2) is shown in the upper (lower) panel. The cross section area of the NW1 and NW2 are 3189.5 Å^2 and 30973.4 Å^2, respectively. These NWs have periodic segments of size $2L_z$, where L_z = 20.435 Å for NW1 and L_z = 61.067 Å for NW2. Gray (green) dots represent indium (phosphorus) atoms. Notice that the twin-planes are composed by alternate layers of different atoms.

constants and bulk modulus at 300 K (the only experimental value available in the literature) by keeping other thermodynamical and structural properties for InP adequately reported before, it is necessary to perform a small modification in a few parameters used in ref 20. Otherwise, the simulations would lead to an underestimation of the elastic constants for bulk InP. Periodic boundary conditions are applied in the *z*-direction with a vacuum region of 60 Å created in the perpendicular directions. The whole system is allowed to relax in order to eliminate stress and is left to attain thermal equilibrium at temperatures close to 0 K.

Figure 1a shows the **NW1** simulated by molecular dynamics, which has a cross section area of 3189.5 Å^2, and a total length of 408.7 Å, totalizing 51 320 atoms (25 660 In + 25 660 P). In Figure 1b we display the results for **NW2**, which is simulated by considering a cross section area of 30973.4 Å^2, and a total length of 366.4 Å, totalizing 449 244 atoms (224 622 In + 224 622 P). Both NWs consist of periodic segments of size $2L_z$, as depicted in Figure 1, where L_z = 20.435 Å for **NW1** and L_z = 61.067 Å for **NW2**. One can notice, in Figure 1, that the twin-plane structure remains after undergoing the thermalization and relaxation processes, which confirms the stability of this configuration. Because of the finite cross section size at the twin-plane, the positions of the atoms at these interfaces are modified. To visualize the deformation induced by the surface of the twin-plane NW, we display in Figure 2 the atomic positions of one species (In), in the deformed plane ⟨111⟩, after the system has undergone the relaxation and thermalization processes. The size of the cross section has a strong influence on this deformation and, depending on surface size, the mere presence of the surface may lead to a distribution of strain over the whole structure. However, in the range of parameters used to simulate the two NWs, the relative strain variation between consecutive core

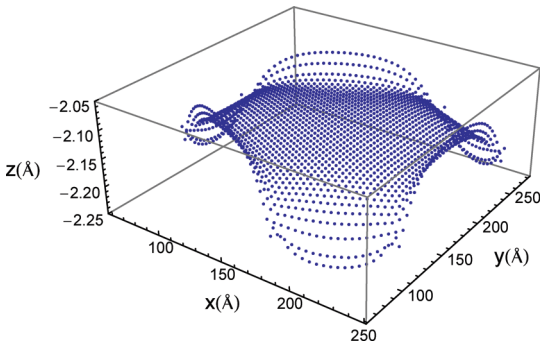

Figure 2. Visualization of a deformed interface of twin-planes in NW2. To emphasize the deformation induced by this surface, only the atomic position of one species is shown: the indium atoms represented by dots at the twin interface.

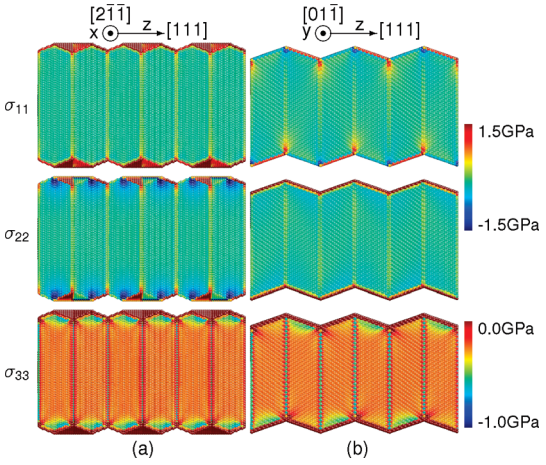

Figure 3. Visualization of the local stress tensor components of the NW2. The left panels correspond to longitudinal cut view in the middle region of the NW2 at the plane [2$\bar{1}\bar{1}$]. The right panels show the stress distribution for cuts at the plane [01$\bar{1}$]. Color coding of stress threshold was saturated at the surface in order to get a better contrast in the central region.

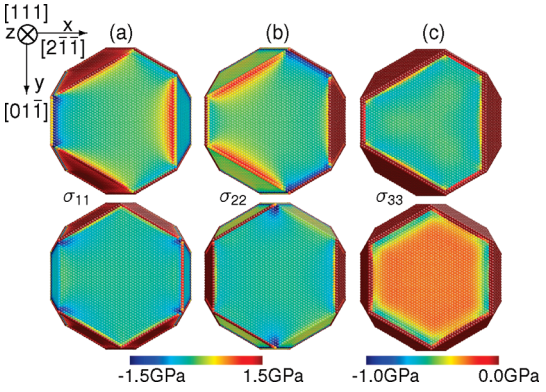

Figure 4. Visualization of the local stress tensor components of the NW2. Upper panels show distribution of stress components for a transversal cut taken at the twin-plane interface. Lower panels show the stress distribution for transversal cuts taken at the middle of the segment. Columns a, b, and c show the distribution of the diagonal components of the stress tensor σ_{11}, σ_{22}, and σ_{33}, respectively.

segments and the interfaces near the twin-planes remains practically unaltered. For this reason, we present the results of strain distribution only for **NW2**, which has a size more compatible with typical experiments.[8,9] Note in Figure 2 that the vertical (z) and horizontal scales (x,y) are not the same in order to better visualize the effects of twin-planes deformation induced by surface effects. The local stress distribution is calculated using the algorithm supplied in ref 21. Because the NW is not uniform, the local stress at the center of the **NW2** is obtained by averaging the computed local stress for 70 atoms within the same plane around each point.

In Figure 3, we plot the distribution of the diagonal components σ_{11}, σ_{22}, and σ_{33} of the stress tensor for a longitudinal cut taken in the middle region of the **NW2**, where the color coding stress threshold is saturated at the surface for a better contrast in the central region. The left panels (Figure 3 a) correspond to [2$\bar{1}\bar{1}$] cut plane view, whereas the right panels (Figure 3b) correspond to the [01$\bar{1}$] cut plane view. Only σ_{11}, σ_{22}, and σ_{33} diagonal stress tensor components reveal the interface influence along the wire, once the off-diagonal stress components have negligible values. In Figure 4, we show the stress distribution for the same components, but for cross section cuts in the **NW2** taken along [111] direction. The top panels display the stress distributions for the cut plane taken at the twin-plane interface and the bottom panels, for cuts taken in the middle of the segment between two consecutive twin-planes. The stress distribution in the region between two twin-planes depends on the NW cross-section size. By increasing the cross section, the influence of the surface on the twin-plane strain field becomes less effective and the stress distribution becomes flat and goes to zero in these regions.

The linear approximation is adequate to characterize the correlation between stress and strain fields in a NW, which is given by Hooke's law: $\sigma'_{ij} = -\mathcal{C}_{ijkl}\varepsilon'_{kl}$, where σ'_{ij} labels a stress tensor component, $-\mathcal{C}_{ijkl}$ is a component of the fourth order elastic stiffness tensor, and ε'_{kl} is the strain tensor component.

To determine the strain tensor components for wires grown as shown in Figure 1, a rotation from ([100],[010],[001]) to ([2$\bar{1}\bar{1}$],[01$\bar{1}$],[111]) crystalline directions was performed. The general relations between new and old coordinate systems are[21] $\sigma_{\alpha\beta} = \mathcal{U}_{i\alpha}\mathcal{U}_{j\beta}\sigma'_{ij}$, $\varepsilon_{\alpha\beta} = \mathcal{U}_{i\alpha}\mathcal{U}_{j\beta}\varepsilon'_{ij}$, $\mathcal{C}_{\gamma\delta kl} = \mathcal{U}_{\alpha\gamma}\mathcal{U}_{\beta\delta}\mathcal{U}_{ik}\mathcal{U}_{jl}\mathcal{C}'_{\alpha\beta ij}$, where the summation over repeated indices is assumed and the elements of the rotational matrix $\mathcal{U}_{mn}$ are given by

$$\mathcal{U} = \begin{pmatrix} \cos\alpha\cos\beta & -\sin\alpha & \cos\alpha\sin\beta \\ \sin\alpha\cos\beta & \cos\alpha & \sin\alpha\sin\beta \\ -\sin\beta & 0 & \cos\beta \end{pmatrix} \quad (1)$$

where $\beta = \arccos(l/(h^2 + k^2 + l^2)^{1/2})$, $\alpha = \arccos(h/(h^2 + k^2)^{1/2})$, and h, k, and l designate the Miller indexes. In the new axis, Hooke's law, can be rewritten as

$$\sigma_{\gamma\delta} = -\mathcal{C}_{\gamma\delta kl}\varepsilon_{kl} \quad (2)$$

that is given in terms of the 36 components of the elastic stiffness tensor,[22]

$$\mathcal{C}_{\gamma\delta kl} = \mathcal{C}_{11}' \sum_{\alpha=1}^{3} \mathcal{U}_{\alpha\gamma}\mathcal{U}_{\alpha\delta}\mathcal{U}_{\alpha k}\mathcal{U}_{\alpha l} + \mathcal{C}_{12}' \sum_{\beta=2}^{3}\sum_{\alpha=1}^{\beta-1} (\mathcal{U}_{\alpha\gamma}\mathcal{U}_{\alpha\delta}\mathcal{U}_{\beta k}\mathcal{U}_{\beta l} + \mathcal{U}_{\beta\gamma}\mathcal{U}_{\beta\delta}\mathcal{U}_{\alpha k}\mathcal{U}_{\alpha l}) + \mathcal{C}_{44}' \sum_{\beta=2}^{3}\sum_{\alpha=1}^{\beta-1} (\mathcal{U}_{\alpha\gamma}\mathcal{U}_{\beta\delta} + \mathcal{U}_{\beta\gamma}\mathcal{U}_{\alpha\delta}) \times (\mathcal{U}_{\alpha k}\mathcal{U}_{\beta l} + \mathcal{U}_{\beta k}\mathcal{U}_{\alpha l}) \quad (3)$$

For materials which crystallize in cubic symmetry, such as the zincblende structure, the stiffness tensor can be reduced from 36 to only 3 nonzero components labeled as $\mathcal{C}_{11}$, $\mathcal{C}_{12}$, and $\mathcal{C}_{44}$ elastic constants.

The electronic structure calculation presented below simulates the system behavior at T = 0 K. However, only room temperature values of the elastic constants are found in the literature.[23] Thus, besides the strain field mapping, our MD simulations is also used to deliver the elastic constants at zero temperature: $\mathcal{C}_{11}'$ = 107.68 GPa, $\mathcal{C}_{12}'$ = 60.65 GPa and $\mathcal{C}_{44}'$ = 41.10 GPa. The six components of the stress tensor along [111] direction as a function of the position is also obtained from the MD calculations. Thus, we use eq 2 to calculate the strain potential profile along this direction. In Figure 5a and Figure 5b, we show the calculated strain distribution for the relaxed **NW2** displayed along its longitudinal direction (by relaxed, we mean a wire not subjected to any external deformation). Two main characteristics can be observed in Figure 5a and Figure 5b: (i) the NW core (plateau regions) appears positively strained in all directions; (ii) drastic fluctuations of strain take place at the twin-plane interfaces. To probe the effects of an external deformation, we apply tension and compression on the **NW2** along the *z*-direction in order to obtain deformations ranging from −1.0% to +1.0% in their longitudinal length at $T \approx 0$ K. The resulting diagonal strain components for the externally strained wires are displayed in Figure 5c,d. Observe in Figure 5c,d that the diagonal strain components perpendicular to the longitudinal direction (ε_{11} and ε_{22}) are shifted to positive (negative) values due to the positive (negative) uniaxial strain applied to the nanowire. On the contrary, the diagonal strain components ε_{33} has an opposite behavior and it is shifted to negative (positive) values under positive (negative) uniaxial applied stress.

Electronic and Transport Properties. The most common superlattices[24] are formed by alternating layers of two different semiconductors. Because different materials have a distinct bandgap, there is a discontinuity in the potential profile at the interfaces. As a result, the electronic structure of a superlattice behaves as a sequence of quantum wells separated by barriers. This

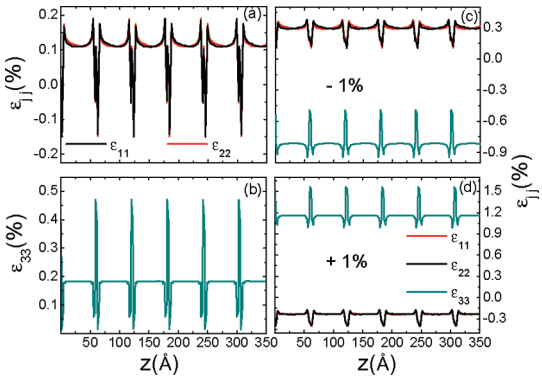

Figure 5. Average values of the central strain distributions along longitudinal direction [111] of the NW2 showing the possible types of twin-plane superlattice structures. Panels a and b correspond to relaxed NW; Panels c and d correspond to externally strained NW. In panel c, the wire is under compression and in panel d, the wire is under tension. In panels c and d, the black line represents the component ε_{11}, the red line represents the component ε_{22}, and the dark cyan line represents the component ε_{33}.

periodic sequence of quantum wells and barriers creates a miniband structure, which is constituted of alternated regions of allowed and forbidden energies. The regions of allowed energies correspond to hybridization of quasi-bound states that are localized between the barriers. Therefore, carriers can efficiently tunnel through the superlattice when their energy reaches these allowed regions and the structure becomes transparent for the electronic transport. Obviously, these phenomena are observed if the quantum wells have a minimum size and height capable of forming quasi-bound states. In addition, the heavier the effective mass of the carrier, the easier the formation of a quasi-bound state.

In this subsection, we use the calculated intrinsic strain fields of NWs, which appear due to the arrangement of atoms during the formation of the wire-shape structure, together with the effects of external deformations to show that twin-planes NWs behave as 1D superlattices. Mainly, the impact of strain fields on the band structure is given by a shift in the conduction and valence-band edges and a split of the degeneracy of the heavy- and light-hole subbands. The influence of strain fields on the effective potential profile for conduction and valence bands can be ascribed to the deformation potentials: *a*, *b*, and *d*.[25] In particular, the effect on the conduction band is isotropic,[26] $H_{cond} = a_c(\varepsilon_{11} + \varepsilon_{22} + \varepsilon_{33})$, where a_c is the conduction-band deformation potential. In turn, the potential profile for the valence band is anisotropic, and a rotation in the Bir−Pikus Hamiltonian[27] should be performed.[28] For the [111] direction, the energy shifts for heavy- and light-hole subbands are respectively $H_h = -a_v(\varepsilon_{11} + \varepsilon_{22} + \varepsilon_{33}) - (d_v/\sqrt{3})(\varepsilon_{11} + \varepsilon_{22} - \varepsilon_{33})$ and $H_l = -a_v(\varepsilon_{11} + \varepsilon_{22} + \varepsilon_{33}) + (d_v/\sqrt{3})(\varepsilon_{11} + \varepsilon_{22} - \varepsilon_{33})$, where the valence band deformation potentials are labeled by a_v and d_v.

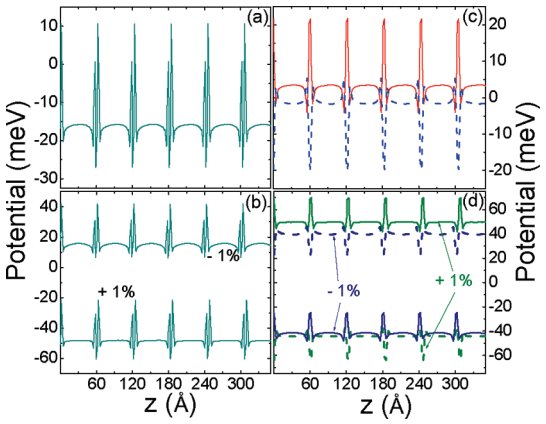

Figure 6. Calculated effective superlattice potential along [111] direction at the NW2 core. Panel a shows the conduction band profile for the relaxed NW2. Panel b shows the conduction band profile for the externally strained NW2, considering the wire subjected to +1% tension (upper trace) and subjected to −1% compression (lower trace). Panel c: valence band profiles for the relaxed NW2. The solid red lines describe the heavy-hole profile and the dashed blue lines describe the light-hole profiles. Panel d: valence band profiles for the externally strained NW2 under +1% tension (upper traces) and for −1% compression (lower traces). In all panels, we adopted the point of view of a valence band electron as the reference to describe the potential profile.

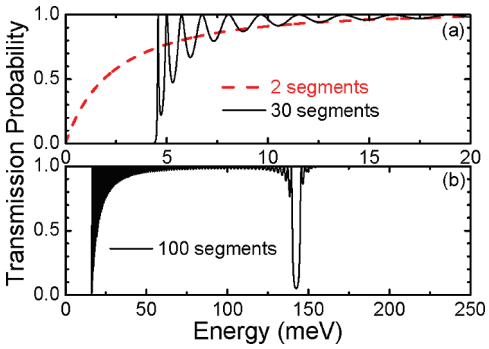

Figure 7. Transmission probability for carriers at the conduction band as a function of the electron energy for NW2, which forms a twin-plane superlattice constituted of (a) 2 (dashed line) and 30 segments (solid line) and (b) 100 segments. The full transparency condition for the system is achieved when the transmission probability reaches 1. In all cases the energy has been measured from the corresponding band minimum.

The calculated potential profile induced by strain for electrons along [111] direction for the relaxed and for the externally strained **NW2** are displayed in Figure 6, panels a and b, respectively. It can be noted in both cases that there are fluctuating potentials at the positions where an interface between the twin-planes occurs. Such fluctuations act as potential barriers for electrons alternated by quantum wells, thus constituting a 1D superlattice. The difference provided by external strain is a shift in the bottom of the conduction band, which is positive (negative) for the compressive (tensile) case. For **NW2**, the thickness of the quantum wells is approximately 45 Å separated by barriers of thickness approximately 15 Å. The potential profiles for **NW1** (results not shown here) and **NW2** are very similar and the only difference between them is related to the size of the barriers and wells. For **NW1**, the thickness of the barriers is approximately 5 Å and the thickness of the quantum wells is close to 15 Å. For both **NW1** and **NW2**, the average height of the barriers have the same value, which is approximately 15 meV (see Figure 6).

For the valence band, we have two distinct situations to consider according to the heavy- or light-hole subband character of the carrier. Here, the profile corresponds to the potential from the point of view of a valence band electron. According to Figure 6c,d, we can observe that the heavy-hole and conduction subbands have similar profiles and follow a sequence of quantum wells separated by barriers (positive fluctuating potentials). On the other hand, the light-hole subband profile presents an inverted sequence of quantum wells (negative fluctuating potentials) and barriers. Therefore, depending on the character of the valence band ground-state, the holes can be confined into different layers of the structure when compared to the electrons at the conduction band. Such a tuning of the ground-state can be performed by applying an external strain (Figure 6d). Also, one can notice, in Figure 6c,d, that the valence band ground-state has a heavy-hole character for both relaxed and under tension (+1%) wires, while the light-hole character dominates for NWs under compression (−1%). As seen in the following discussion, this alternation also affects the transport properties of the NWs.

To characterize carrier transport properties in the 1D superlattice described by the calculated potential profiles, we use the formalism based on the transfer matrix method.[18] The transmission probability was calculated for different combinations of wire sizes and strain configurations. In this work, we consider the transport of both type of carriers: electrons at the bottom of the conduction band and holes at the top of the valence band. In Figure 7, the transmission probability for electrons at the conduction band of the **NW2** is displayed considering different number of superlattice segments. Also, one can observe in Figure 7a and Figure 7b that transmission probability is very close to 1 when the electron energy is higher than 15 meV. Such a result indicates that the twin-plane superlattice is almost fully transparent for electrons. Because the external strain only shifts the conduction band edge (see eq 2), we can affirm that the transmission probability for electrons does not depend on the external deformation. The effects of the potential profile are stronger when the electron energy is smaller than 20 meV. In this case, we can observe quantum interference features (see Figure 6) depending on the number of segments, but there is no observation of a resonant peak due to the small electron effective mass. The qualitative picture for electron transmission

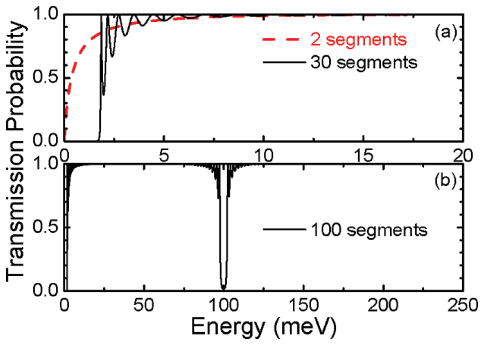

Figure 8. Transmission probability for carriers at the top of the valence band as a function of the hole energy for the NW2 under compression. The twin-plane superlattice consists of (a) 2 (dashed line) and 30 segments (solid line) and (b) 100 segments. The full transparency condition occurs when the transmission probability is equal to 1. In all cases the energy has been measured from the corresponding band minimum.

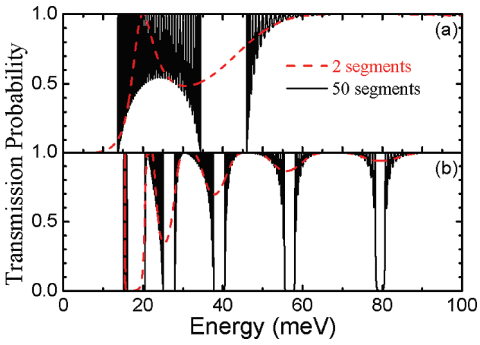

Figure 9. Transmission probability for carriers at the top of the valence band as a function of the hole energy for relaxed or under tension NWs: (a) for the NW1 and (b) for the NW2. The dashed (solid) line is the transmission for a NW composed of 2 (50) segments. The full transparency condition occurs when the transmission probability is equal to 1. In all cases the energy has been measured from the corresponding band minimum.

probability for both **NW1** (results are not shown here) and **NW2** is practically the same. This conclusion comes from the fact that the electronic structure of both NWs only differs from each other by the thickness of the quantum wells and barriers. Therefore, if there is no quasi-bound state for wider quantum wells (**NW2**), there will not be one for narrower wells (**NW1**).

In contrast, the transmission probability for holes at the valence band can be effectively modified by applying an external strain, as depicted in Figure 8 and Figure 9. In both figures, **NW1** and **NW2** were probed by increasing the number of twin-plane segments. When the NW is subjected to compression (Figure 8), the light-hole is the preferential type of carrier and the transparency of the superlattice is evident, since the transmission probability is close to 1 and there is no observation of a resonant peak. Again, this effect is a characteristic of the small mass of this type of carrier. The transmission probability is also quite similar for **NW1** (results are not shown here) and **NW2**, when the NWs are under compression. On the other hand, clear resonant transmission conditions are achieved for either relaxed NWs or under tensile stress, because now the heavy-hole is the preferential carrier type. For the **NW1**, we observe only one sharp peak at the energy ~20 meV (Figure 9a). Alternatively, for the **NW2**, two very sharp peaks in Figure 9b can be noticed, with energies at ~15.5 meV and ~22 meV, respectively. In these both cases, the states with the heaviest mass along the [111] direction are promoted to the top of the valence band (ground-state) and the full transparency of the twin-plane superlattice is no longer observed. Thus, transparent energy bands are alternated between opaque energy gaps. According to the number of twin-plane segments, the transparency contrast can be enhanced as shown in Figure 7.

SUMMARY

The transport properties can be tuned in twin-plane superlattices within semiconductor NWs even in the case of the Γ-electrons of zincblende like systems in contrast to the apparent transparency expected for 2D heterostructures.[5] The application of external stress or any other mechanism that induces strain, such as temperature,[25] can be an effective tool to reach alternate conditions between almost full transparency and opaqueness. The increment of twin-plane segments is definitively a way of increasing the contrast between these situations. To conclude, we have shown that the application of twin-plane superlattices as active parts of nanocircuits can be successfully achieved if the external control of such strain dependency is mastered.

METHODS

We employ parallel computation to integrate the hundreds of thousand Newton's equations of motion for a set of interacting particles. The simulation of the InP compound was carried out by using a many-body potential built by a combination of a two- and a three-body interatomic potentials. The two-body term takes into account steric repulsion due to finite size of the atoms; Coulomb interactions, due to charge transfer between ions; and charge-induced dipole, due to large polarizability of anions and dipole−dipole (van der Waals) attractions. The three-body interaction considers bond bending as well as the bond stretching necessary to model the covalent behavior.[19,20] For the band structure calculations we applied the envelope function approximation within the $\mathbf{k}\cdot\mathbf{p}$ model.[25] The deformation potentials used in the calculations, $a_c = -6.0$ eV, $a_v = -0.6$ eV, and $d_v = -5.0$ eV, were taken from ref 29. The transmission probability was calculated by employing the transfer matrix method,[18] where we approximate the potential profiles by using the energy minimum as reference and the fluctuating potential by a superlattice constituted by barriers with constant heights (15 meV) and constant thickness (15 Å for **NW1** and 5 Å for **NW2**) separated by quantum wells of thickness 45 Å for **NW1** and 15 Å for **NW2**.

Acknowledgment. The authors acknowledge the financial support of Brazilian agencies: CAPES, CNPQ, and FAPESP.

REFERENCES AND NOTES

1. Duan, X.; Huang, Y.; Agarwal, R.; Lieber, C. M. Single-Nanowire Electrically Driven Lasers. *Nature* **2003**, *421*, 241–245.
2. Nilsson, H. A.; Thelander, C.; Fröberg, L. E.; Wagner, J. B.; Samuelson, L. Nanowire-Based Multiple Quantum Dot Memory. *Appl. Phys. Lett.* **2006**, *89*, 163101.
3. Villegas-Lelovsky, L.; Trallero-Giner, C.; Rebello Sousa Dias, M.; Lopez-Richard, V.; Marques, G. E. Spin Polarization in Quantum Wires: Influence of Dresselhaus Spin−Orbit Interaction and Cross-Section Effects. *Phys. Rev. B* **2009**, *79*, 155306.
4. Lopez-Richard, V.; González, J. C.; Matinaga, F. M.; Trallero-Giner, C.; Ribeiro, E.; Sousa Dias, M. R.; Villegas-Lelovsky, L.; Marques, G. E. Markovian and Non-Markovian Light-Emission Channels in Strained Quantum Wires. *Nano Lett.* **2009**, *9*, 3129–3136.
5. Stiles, M. D.; Hamann, D. R. Ballistic Electron Transmission through Interfaces. *Phys. Rev. B* **1988**, *38*, 2021–2037.
6. Ikonic′, Z.; Srivastava, G. P.; Inkson, J. C. Electronic Structure of Twinning Superlattices. *Surf. Sci.* **1994**, *307−309*, 880–884.
7. Ikonic′, Z.; Srivastava, G. P.; Inkson, J. C. Electronic Properties of Twin Boundaries and Twinning Superlattices in Diamond-Type and Zinc-Blende-Type Semiconductors. *Phys. Rev. B* **1993**, *48*, 17181–17193.
8. Caroff, P.; Dick, K. A.; Johansson, J.; Messing, M. E.; Deppert, K.; Samuelson, L. Controlled Polytypic and Twin-Plane Superlattices in III−V Nanowires. *Nat. Nanotechnol.* **2009**, *4*, 50–55.
9. Algra, R. E.; Verheijen, M. A.; Borgström, M. T.; Feiner, L. F.; Immink, G.; van Enckevort, W. J. P.; Vlieg, E.; Bakkers, E. P. A. M. Twinning Superlattices in Indium Phosphide Nanowires. *Nature* **2008**, *456*, 369–372.
10. Schmidt, T. M.; Miwa, R. H.; Venezuela, P.; Fazzio, A. Stability and Electronic Confinement of Free-Standing InP Nanowires: *Ab Initio* Calculations. *Phys. Rev. B* **2005**, *72*, 193404.
11. Miwa, R. H.; Schmidt, T. M.; Fazzio, A. EL2-Like Defects in InP Nanowires: An *ab Initio* Total Energy Investigation. *Phys. Rev. B* **2007**, *75*, 165324.
12. Schmidt, T. M. Hydrogen and Oxygen on InP Nanowire Surfaces. *Appl. Phys. Lett.* **2006**, *89*, 123117.
13. Akiyama, T.; Nakamura, K.; Ito, T. Structural Stability and Electronic Structures of InP Nanowires: Role of Surface Dangling Bonds on Nanowire Facets. *Phys. Rev. B* **2006**, *73*, 235308.
14. Sano, K.; Akiyama, T.; Nakamura, K.; Ito, T. A Monte-Carlo Simulation Study of Twinning Formation in InP Nanowires. *J. Cryst. Growth* **2007**, *301*, 862–865.
15. Persson, M. P.; Xu, H. Q. Electronic Structure of [100]-Oriented Free-Standing InAs And InP Nanowires with Square and Rectangular Cross Sections. *Phys. Rev. B* **2006**, *73*, 125346.
16. Akiyama, T.; Yamashita, T.; Nakamura, K.; Ito, T. Band Alignment Tuning in Twin-Plane Superlattices of Semiconductor Nanowires. *Nano Lett.* **2010**, *10*, 4614–4618.
17. Li, D.; Wang, Z.; Gao, F. First-Principles Study of the Electronic Properties of Wurtzite, Zinc-Blende, and Twinned InP Nanowires. *Nanotechnology* **2010**, *21*, 505709.
18. Bittencourt, A. C. R.; Cohen, A. M.; Marques, G. E. Strain-Induced Enhancement of Resonant Current of Holes in Multilayered Heterostructures. *Phys. Rev. B* **1998**, *57*, 4525–4543.
19. Ebbsjö, I.; Kalia, R. K.; Nakano, A.; Rino, J. P.; Vashishta, P. Topology of Amorphous Gallium Arsenide on Intermediate Length Scales: A Molecular Dynamics Study. *J. Appl. Phys.* **2000**, *87*, 7708–7711.
20. Branicio, P. S.; Rino, J. P.; Gan, C. K.; Tsuzuki, H. Interaction Potential for Indium Phosphide: A Molecular Dynamics and First-Principles Study of the Elastic Constants, Generalized Stacking Fault and Surface Energies. *J. Phys.: Condens. Matter* **2009**, *21*, 095002.
21. Nye, J. F. *Physical Properties of Crystals: Their Representation by Tensors and Matrices*; Oxford University Press: New York, 1985.
22. Hinckley, J. M.; Singh, J. Influence of Substrate Composition and Crystallographic Orientation on the Band Structure of Pseudomorphic Si−Ge Alloy Films. *Phys. Rev. B* **1990**, *42*, 3546–3566.
23. Madelung, O.; Rössler, U.; Schulz, M. *Landolt-Börnstein - Group III Condensed Matter Numerical Data and Functional Relationships in Science and Technology*; Springer: New York, 2001; Vol. 41A1a.
24. Tsu, R. *Superlattice to Nanoelectronics*; Elsevier: Amsterdam, The Netherlands, 2005.
25. Cesar, D. F.; Teodoro, M. D.; Tsuzuki, H.; Lopez-Richard, V.; Marques, G. E.; Rino, J. P.; Lourenço, S. A.; Marega, E., Jr.; Dias, I. F. L.; Duarte, J. L.; *et al.* Contrasting LH−HH Subband Splitting of Strained Quantum Wells Grown along [001] and [113] Directions. *Phys. Rev. B* **2010**, *81*, 233301.
26. Janssens, K. L.; Partoens, B.; Peeters, F. M. Effect of Strain on the Magnetoexciton Ground State in InP/$Ga_xIn_{1-x}P$ Quantum Disks. *Phys. Rev. B* **2003**, *67*, 235325.
27. Pikus, G. E.; Bir, G. L. Effect of Deformation on the Energy Spectrum and the Electrical Properties of Imperfect Germanium and Silicon. *Sov. Phys. Solid State* **1959**, *1*, 136–138.
28. Fishman, G. Hole Subbands in Strained Quantum-Well Semiconductors in [*hhk*] Directions. *Phys. Rev. B* **1995**, *52*, 11132–11143.
29. Vurgaftman, I.; Meyer, J. R.; Ram-Mohan, L. R. Band Parameters for III−V Compound Semiconductors and Their Alloys. *J. Appl. Phys.* **2001**, *89*, 5815–5875.